Journal of CO2 Utilization 107 (2026) 103434

Contents lists available at ScienceDirect

Journal of CO2 Utilization

journal homepage: www.elsevier.com/locate/jcou

CO_2 capture and zeolite synthesis via hydrothermal treatment of inertized rock wool

Giulio Galamini [a,*], Daniele Malferrari [a,b,**], Alessandro Francesco Gualtieri [a,b]

[a] Department of Chemical and Geological Sciences, University of Modena and Reggio Emilia (UNIMORE), via G. Campi 103, Modena 41125, Italy
[b] Inter-Departmental Research and Innovation Centre on Construction and Environmental Services of the University of Modena and Reggio Emilia, Via P. Vivarelli 10, Modena I-41125, Italy

ARTICLE INFO

Keywords:
Sustainable waste upcycling
Mineral carbonation
Hydrothermal zeolite synthesis
Inertized rock wool
Glass product valorisation

ABSTRACT

The management of rock wool waste poses a growing challenge, with global production exceeding 2.5 million tons annually. Thermal inertization converts this fibrous hazardous waste into safe glassy products; however, high-value applications of the inerted product remain limited. This study is a preliminary investigation into a sustainable valorization pathway for thermally inertized mineral wool, focusing on CO_2 recovery during low-temperature (130 °C) alkaline hydrothermal synthesis. A comparative assessment was performed between synthesis in a CO_2-enriched atmosphere and ambient air. Results revealed CO_2 as a key parameter controlling crystallization pathways and zeolite yield, along with CO_2 fixation through carbonation. Synthesis in air predominantly yielded 11-Å tobermorite and transient carbonates (vaterite), with limited zeolite (analcime) formation. Conversely, the CO_2-enriched atmosphere suppressed tobermorite, favoring Na-P and phillipsite zeolites alongside stable calcite. The CO_2-based process proved superior across all key metrics. Zeolitic yields were nearly fourfold higher, resulting in a cation exchange capacity of 40.7 ± 1.6 compared to 12.3 ± 0.9 cmol(+)/kg in air. Furthermore, CO_2-synthesis demonstrated an 86% increase in carbon capture efficiency (4.49 wt% vs. 2.41 wt%), driven by stable mineral carbonation. Overall, the proposed hydrothermal pathway provides a promising laboratory-scale strategy for *End-of-Waste* upcycling while enabling CO_2 sequestration, demonstrating that a CO_2-rich environment enhances zeolite crystallization and increases CO_2 retention.

1. Introduction

Rock wool is widely used for thermal and acoustic insulation. However, upon reaching the end of its service life, it is classified as hazardous waste in the EU. The main reason lies in their high content in amorphous silicate glass fibres, specifically respirable fractions, with dimensional criteria defined by the Worl Health Organization [1]. Thermal inertization offers the advantage of recovering the material, thereby enabling its potential reuse as a recycled product and contributing to environmental sustainability goals as defined by the European Green Deal and the 2030 Agenda [2]. The thermal inertization involves treatments reaching temperatures high enough to induce profound transformations that destroy the fibrous fraction, resulting in a dense, glassy material known as RE.WO (acronym derived from the LIFE22-ENV-IT-LIFE ReWo project: 'REcycling mineral WOol waste into high-value products' [3,4]). Despite the technological readiness level achieved, this procedure has limited application yet. Among the main reasons, alongside legislative and bureaucratic issues, there is the difficulty in defining possible fields of use for RE.WO. Therefore, without applicative scenarios, this material, although inert, remains a non-hazardous waste to dispose of.

The recent research on the possible applications of RE.WO includes the formulation of ceramic glazes. Indeed, due to its elevated CaO content (approximately 16 wt%), the RE.WO can act as a high-temperature flux, compatible with firing conditions typical of stoneware and porcelain stoneware. Its substantial amounts of SiO_2 (≈ 45 wt %) and Al_2O_3 (≈ 13 wt%) also contribute to the vitrification of the glaze, and the relatively high Fe_2O_3 content (≈ 10 wt%) functions as a chromophore, imparting light to dark brown hues on the glaze [5]. RE.WO has been employed as a component in the production of porcelain

* Corresponding author.
** Corresponding author at: Department of Chemical and Geological Sciences, University of Modena and Reggio Emilia (UNIMORE), via G. Campi 103, Modena 41125, Italy.
E-mail addresses: giulio.galamini@unimore.it (G. Galamini), daniele.malferrari@unimore.it (D. Malferrari).

https://doi.org/10.1016/j.jcou.2026.103434
Received 16 February 2026; Received in revised form 19 April 2026; Accepted 20 April 2026
Available online 27 April 2026

stoneware ceramic bodies, demonstrating its potential for use in tile manufacturing, meeting the required mechanical performance parameters. In this case as well, the Fe content induces dark coloration in the body, an aesthetic feature that may nonetheless be of interest for certain market segments [3].

An unexplored pathway for the valorization of RE.WO is using it as a precursor of useful microporous minerals in a synthesis process. Its chemical composition is indeed characterized by high Si, Al, and Ca contents, making it a potentially ideal precursor for the synthesis of zeolites.

Zeolites are crystalline aluminosilicates defined by three-dimensional frameworks of $[SiO_4]^{4-}$ tetrahedra, creating a microporous network of interconnected channels and cages [6]. The isomorphous substitution of Si^{4+} with Al^{3+} within the tetrahedral lattice generates $[AlO_4]^{5-}$ units that impart a net negative charge to the framework. Electroneutrality is therefore achieved by the occurrence of loosely bound, therefore exchangeable, cations located within the microporous structure. This configuration confers specific properties to zeolites, including molecular sieving, reversible hydration, and, most notably, high cation exchange capacities (CEC). CEC enables the exchange of extra-framework cations, with ions present in an external solution, usually referred to as counterions [7].

While traditional literature primarily focused on the synthesis of zeolites using high-purity reagents to ensure idealized replicable conditions, recent research has shifted toward a waste-to-zeolite strategy, aligning with circular economy principles that seek to transform industrial by-products into high-value functional materials [8]. Coal fly ashes from thermoelectric plants are widely used as feedstocks for these syntheses [9,10], as are metallurgical slags [11,12] and waste glass [13,14]. Other precursors are, i.e., red mud [15], basalt waste [16], and bauxite residues [17], often successfully converted into valuable zeolite products. Agricultural residues are used as well for the synthesis of valuable zeolites. In example, mordenite has been synthesized from rice husk ash as a silica source, eliminating the need for expensive organic structure-directing agents [18].

Hydrothermal alkaline conversion remains the most established method in this field, as it facilitates the dissolution of the precursors followed by the controlled crystallization of zeolitic frameworks. Other methods involve the use of microwave irradiation, to increase the velocity of the synthesis and obtain purer products. Indeed, zeolites have been synthesized from municipal solid waste incineration ashes using microwave-assisted hydrothermal synthesis [19]. Moreover, combined microwave and ultrasonic irradiation have been used to synthesise pure Y zeolite from coal fly ash [20]. The products obtained are usable in many critical applications like the removal of heavy metals in water and wastewater treatment plants [21], to recover NH_4^+ [22] or dye residues [23]. When suitably modified, zeolites are effective in removing organic molecules and anions [24,25]. Other applications involve their capacity to adsorb polar and polarizable gaseous species such as NH_3, CO_2, NO_x, as well as sulfonated and fluorinated gases [26–29], allowing their separation and storage. Due to their capacity to retain and gradually release specific chemical species and ions, natural zeolites (i.e., rocks naturally enriched in zeolitic minerals) are employed in many agricultural applications, for instance as a repellent for pathogenic insects [30], as soil amendments [31], or as key components in fertilizers [32,33].

A problem in the production of RE.WO, as well as other glasses produced through *End-of-Waste* cycles, concerns CO_2 emissions during thermal treatments. One of the most common methods for sequestering CO_2 in these systems involves the mineralization of CO_2 as stable carbonates. CO_2 fixation through carbonation is widely acknowledged as a key pathway for providing stable and permanent greenhouse gas storage [34], in accordance with the Paris Agreement [35] and recent guidelines from the IPCC [36], and IEA [37]. Moreover, research on CO_2 fixation is shifting from natural mineral sources toward industrial wastes. Indeed, the latter is a highly attractive strategy as it simultaneously addresses carbon sequestration requirements and the valorization of wastes, by-products, and materials derived from *End-of-Waste* processes [38]. Thin-film reactors [39] and microwave irradiation [40] have been implemented to increase carbonation of steel and electric arc furnace slags. Carbonation of steel slag has been successfully tested for the sequestration of CO_2 from flue gas [41].

Despite the extensive literature on zeolite synthesis from waste materials and mineral carbonation, these two aspects are usually investigated as separate processes. Their integration and possible synergistic effects in hydrothermal systems is indeed a largely unexplored path and a significant knowledge gap exists regarding how a reactive, CO_2-enriched atmosphere interacts with the alkaline hydrothermal environment during zeolite synthesis. Recent pioneering studies explored this intersection, primarily relying on sequential multi-step processes. For example, Hu et al. [42] developed a method where calcium and magnesium were first extracted from metallurgical slags for CO_2 sequestration, while the remaining silicon- and aluminum-rich solution was subsequently used to synthesize faujasite zeolites. Shin and Kim [43] demonstrated the synthesis of P-type zeolite utilizing the solid residues left over after the indirect carbonation of coal fly ash. However, the combined and single-step hydrothermal synthesis of zeolites in a CO_2-enriched atmosphere to actively steer phase crystallization and carbon fixation remains a highly innovative and largely unexplored field.

This study introduces an integrated approach aiming at the simultaneous synthesis of zeolitic phases and CO_2 fixation, exploring the control of a CO_2-enriched atmosphere toward the crystallization pathways of zeolites in hydrothermal syntheses. By comparatively investigating the hydrothermal conversion of RE.WO under standard ambient air (hereafter referred to as AIR synthesis) and a CO_2-enriched atmosphere (CO_2 synthesis), this work provides evidence of the effects of the CO_2 atmosphere in regulating the production of both zeolites and carbonate species evolving from RE.WO.

The products derived from the syntheses are characterized, as well as their extent of CO_2 enrichment, the morphological and chemical characteristics, and the CEC. To minimize energy consumption, the system was evaluated under mild hydrothermal conditions (130 °C) without the addition of reagents or catalysts other than NaOH. In this regard, the modest thermal requirements could be sustainably satisfied by recovering waste heat from the inertization stage itself, which operates at temperatures exceeding 1000 °C [3].

This approach not only offers a new valorization pathway for *End-of-Waste* products but also closes the loop by directly mitigating the carbon footprint of the inertization process itself.

2. Materials and methods

2.1. Characterization of the RE.WO

RE.WO was mechanically milled to optimize the synthesis. To evaluate the particle size distribution, the resulting powder, hereafter referred to as RE.WO_PRE, was analysed via laser diffraction (Mastersizer 3000, Malvern Panalytical, Worcestershire, UK) following standard procedure [44]. The characteristic volumetric diameters were as follows: Dv10 = 4.53 μm, Dv50 = 24.8 μm, and Dv90 = 62.0 μm. The distribution span was calculated as 2.31.

The chemical characterization of the RE.WO_PRE and selected synthesis products was measured in acid digested samples by ICP-MS (iCAP TQ, Thermo Fisher Scientific, Waltham, MA, USA) with three replicates each. The mineralization process involved a sequential acid digestion at 200 °C as follows. About 0.1 g dry mass was mixed with 30 ml of 65% HNO_3, 15 ml of 40% HF, and 5 ml of 37% HCl. The samples were then evaporated to dryness and re-dissolved three times to eliminate any traces of HF, using 30 ml of 2% HNO_3 for each dissolution. The final weight of the liquid samples was recorded and used in the correction of the measured concentrations. Digested samples were analysed using a triple quadrupole inductively coupled plasma mass spectrometer (ICP-

MS; iCAP TQ; Thermo Fisher Scientific). The results of the chemical analysis of the starting material (RE.WO_PRE), compared with selected samples from the syntheses in air and CO_2, are reported in 3.5.

To quantify the potential of C capture and the CEC, the total C and N contents of RE.WO_PRE and two selected synthesis products (AIR_96 and CO_2_96) were quantified by Elemental Analysis (EA) with a Vario Micro Cube Elemental Analyser (Elementar, Langenselbold, Germany) (see 2.4 for further details). Si and Al of RE.WO_PRE and selected synthesis products were measured in loose powdery samples by Wavelength Dispersive X-Ray Fluorescence spectrometry (WDXRF; Zetium, Malvern Panalytical, UK).

2.2. Synthesis batches

AIR and CO_2 synthesis were carried out following these steps: 1) aliquots of 15 ml of 1 M NaOH were added to 1 g of RE.WO_PRE into cylindrical Teflon vessels; 2) Vessels were sealed and placed in oven at 130 °C under continuous stirring; 3) Vessels were removed from the oven at distinct times, allowing to evaluate phase dissolution and crystallization kinetics, namely after 24, 48, 72, and 96 h.

To enrich the atmosphere with CO_2, the vessels of the CO_2 batch were placed without the cup in an airtight bag along with a CO_2 canister. Air was evacuated with a vacuum pump and replaced with CO_2 by opening the canister's valve. After sealing, the vessels were removed from the CO_2-saturated bag and put in the oven as described above.

The synthesis products were recovered by filtration and thoroughly washed with deionized water to remove the residual NaOH and soluble reaction products. After washing, the solids were dried at 105 °C for 24 h before further characterization.

Collected samples are referred hereafter as follows: AIR_24, AIR_48, AIR_72, and AIR_96, for the AIR-based synthesis, and CO_2_24, CO_2_48, CO_2_72, and CO_2_96, for the CO_2-based synthesis, at 24, 48, 72, and 96 h, respectively.

2.3. Mineralogical and morphological characterization of the products

The mineralogical composition of the products was assessed by X-ray Powder Diffraction (XRPD) using a X'Pert PRO diffractometer (Malvern Panalytical, UK) equipped with a Real Time Multiple Strip (RTMS) detector, featuring a PSD length of 2.12° 2θ. The incident beam consisted of Cu Kα radiation (λ = 1.5406 Å) operated at 40 kV and 30 mA, with a nickel filter. On the incident beam, a 0.02 rad Soller slits, 10 mm anti-scatter mask, and 1/4° divergence and anti-scatter slits were used. On the diffracted beam path, a 5.0 mm anti-scatter mask and 0.02 rad Soller slit were employed. Data were collected in continuous scan mode with an integration time of 400 s and a step size of 0.0170° 2θ. The scanning range was 3–90° 2θ.

Quantitative phase analyses (QPA) were carried out by the Rietveld refinement method, using NIST SRM 676a (alumina powder, corundum structure) as internal standard. Refinements were performed using the GSAS software package [45] with EXPGUI as graphical interface [46], following the protocol described by Gualtieri et al. [47].

The morphology of the synthesis products and elemental investigations were investigated with a Field Emission Gun Scanning Electron Microscope (FEG-SEM; Nova NanoSEM FEI 450, Thermo Fisher Scientific, Massachusetts, USA) equipped with a XEDS Bruker QUANTAX-200 detector. The samples used were mounted on aluminium stubs previously covered with carbon-conductive adhesive tape and coated with graphite. Observations were performed in high vacuum mode with an accelerating voltage between 15 and 25 keV for both imaging and semiquantitative analyses.

2.4. Chemical characterization and cation exchange capacity

To verify possible chemical differentiations between RE.WO_PRE and syntheses products, selected samples (AIR_96 and CO_2_96) were digested in triplicates and analysed by ICP-MS (iCAP TQ; Thermo Fisher Scientific) using the same procedure explained in 2.1.

An attempt was made to quantify the CEC through ion displacement using NH_4Ac following the Hendershot and Duquette method [48]; however, the dissolution of solid phases prevented an accurate quantification. Consequently, the CEC was determined by analysing the total nitrogen (N, representative of the NH_4^+-N content) through EA technique, following multiple washings with ethanol to remove the excess of the NH_4Ac solution. Nevertheless, the concentrations of the main cations released by RE.WO_PRE, AIR_96, and CO_2_96 in the NH_4Ac solution were still measured by ICP-MS, as they provided an indication of the release of important elements in aqueous media.

3. Results and discussion

3.1. Mineralogical characterization and crystallization kinetics of the synthesis products in air

The XRPD patterns and QPA results of the RE.WO_PRE and the AIR and CO_2 syntheses are shown in Fig. 1 and Table 1, respectively. The mineralogical evolution of RE.WO_PRE throughout the syntheses is shown in Fig. 2. One of the most important phases obtained in the synthesis carried out in air, was tobermorite. The basal peak (002) appeared at 2θ = 7.75°, consistent with 11-Å tobermorite, thermally stable at the synthesis temperature of 130 °C [49–51]. In the CO_2 system, the (002) reflection of tobermorite (samples at 48 and 96 h) shifts to a slightly higher 2θ value (~8.16°), indicating a more pronounced contraction of the interlayer spacing. Plausibly, this shift was due to the partial decalcification of tobermorite induced by CO_2, and carbonation reaction, as evidenced by the presence of calcite in the samples obtained in the CO_2 enriched atmosphere. As observed in the SEM-FEG images, tobermorite in AIR was pervasive, with its characteristic lamellar habit, and completely coated the material grains (Fig. 3).

Calcium carbonate ($CaCO_3$) formed as a mixture of the polymorphs calcite and vaterite; notably, the latter was detected only in the AIR syntheses. As a metastable polymorph, vaterite possesses a complex crystallographic nature, typically reported in monoclinic, orthorhombic, or hexagonal symmetry systems. Its presence suggests a specific kinetic pathway in the air-based system that was likely bypassed in the CO_2 environment. As mentioned, the discriminant for the crystallization of vaterite was the CO_2. It is plausible that at higher CO_2 partial pressures (as in the CO_2-based syntheses), the carbonation process was more efficient, leading directly to the formation of stable calcite, without the presence of vaterite. Conversely, in the air-based synthesis, where CO_2 partial pressure was significantly lower, vaterite was dominant with respect to calcite. However, both calcite and vaterite were transient phases in the AIR syntheses, as after 96 h they completely disappeared. In summary, the AIR synthesis followed a multistage reaction pathway with 11-Å tobermorite that progressively increased at the expense of both the glass matrix and the carbonate phases (calcite and vaterite), as metastable precursors. Notably, since the elemental carbon content of RE.WO_PRE was negligible, the carbonate formation in the air-equilibrated system was nearly entirely dependent on exogenous CO_2 sequestered from the Teflon vessel's headspace. This confirms that the synthesis process can capture CO_2 present in the reactor headspace (air-equilibrated) even in the absence of an enriched gas source.

Analcime was the only zeolite observed in the AIR synthesis. It was obtained in limited amounts, with a maximum of approximately 2.4 wt % after 96 h (Table 1). Jiménez et al. [52] report that higher amounts of analcime, relative to tobermorites, can be obtained at a lower NaOH concentration of 0.5 M compared to 1, 2 and 3 M. In the same study, tobermorite was the primary phase obtained.

Tobermorites typically exhibit a Ca/Si molar ratio between 0.80 and 0.85 [53,54]. The RE.WO_PRE has a high Ca content of approximately 16.6 wt%, with Ca/Si at about 0.52. Therefore, the favorable Ca/Si ratio in AIR likely promoted the precipitation of tobermorite over analcime.

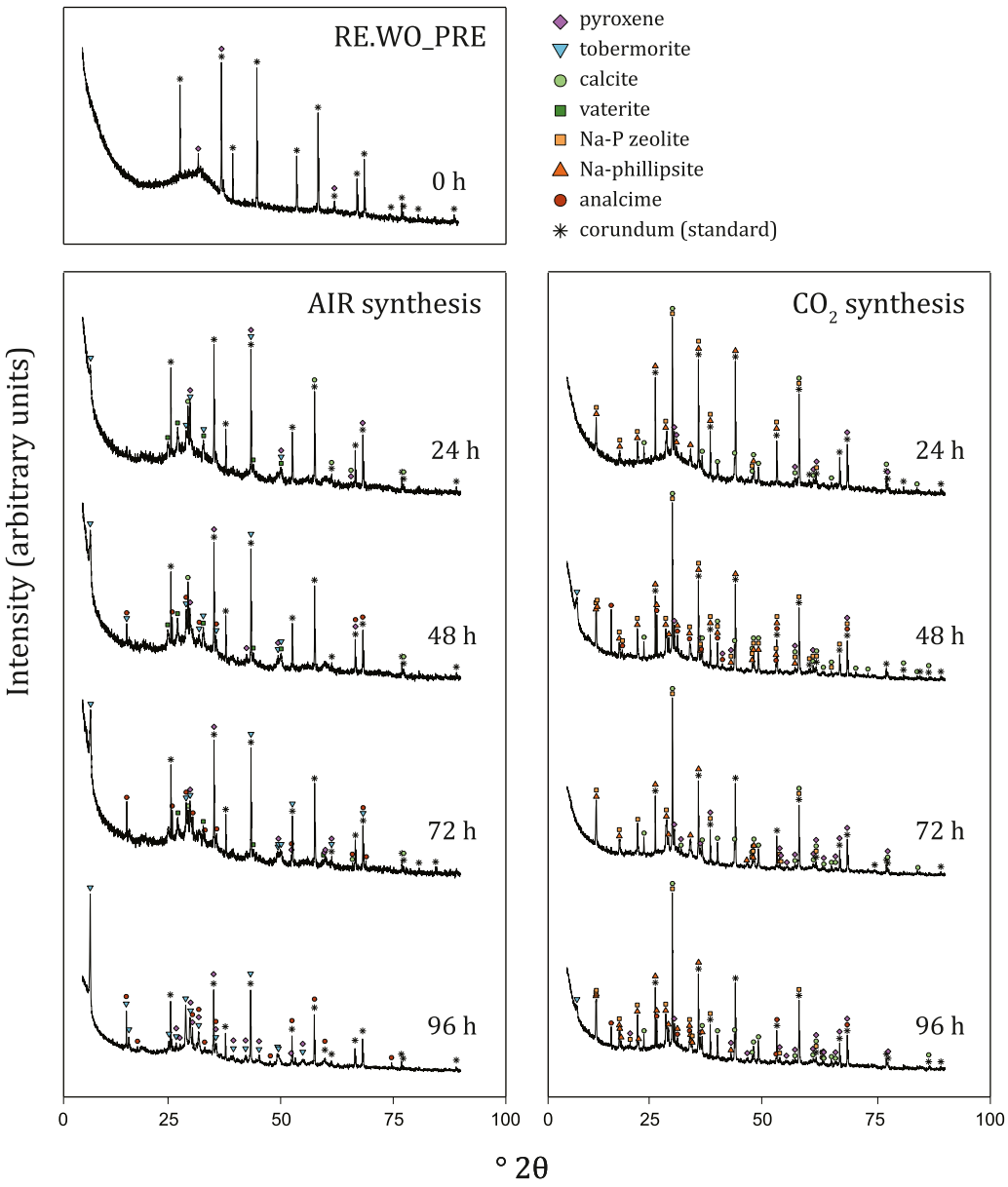

Fig. 1. XRPD patterns of the RE.WO_PRE and the synthesis products (AIR and CO_2) after 24, 48, 72 and 96 h. Symbols represent the main peaks of the detected phases (Table 1) and of the internal standard NIST SRM 676a (alumina powder, corundum structure). Symbols are as follows: purple diamond, pyroxene; blue triangle down, tobermorite; light green circle, calcite; green square, vaterite; yellow square, Na-P zeolite; orange triangle up, Na-phillipsite; red circle, analcime; asterisk, corundum (standard).

SEM-FEG point analyses revealed Fe concentrations within the analcime crystals up to 6.3 wt%. Therefore, the obtained analcime was likely partially Fe-substituted, a concrete scenario supported by the high Fe content in RE.WO_PRE (~ 8.5 wt%). It is well-established that Fe^{3+} can be incorporated into the analcime framework via isomorphous substitution of Al^{3+} [55]. Given the larger ionic radii of Fe^{3+} compared to Al^{3+} (0.49 and 0.39 Å in tetrahedral coordination), this substitution induces a measurable lattice expansion. This trend is corroborated by XRPD data; a comparison between the d-spacings reported in [55] (Fe/(Fe+Al) = 0.2) and those obtained in this study for the RE.WO_PRE sample (Fe/(Fe+Al) = 0.5) reveals a shift towards higher d-values. Specifically, the d-spacings of the (211), (400) and (332) reflections increased from 5.59, 3.43, and 2.92 Å [55] to 5.60, 3.44, and 2.93 Å (AIR_96 sample), respectively, confirming the expansion of the unit cell dimensions with increasing iron content.

3.2. Mineralogical characterization and crystallization kinetics of the synthesis products in CO_2

In AIR, vaterite was dominant relative to calcite. In the CO_2 synthesis instead, only calcite was observed (Table 1 and Fig. 2). Moreover, while carbonates in the AIR synthesis were transient phases that completely dissolved after 96 h, calcite obtained in CO_2 persisted throughout the incubation period. Plausibly, the presence of vaterite in AIR indicates that the system was in an intermediate metastable stage [56], whereas in the CO_2-based synthesis, the crystallization kinetics towards the stable calcite was significantly accelerated [57].

In the AIR syntheses, tobermorite was a dominant and stable phase, alongside analcime and pyroxene (the latter derived from the RE.WO_PRE). Conversely, under CO_2 atmosphere, tobermorite was identified only as a transient accessory phase, as it was detected by XRPD only after 48 and 96 h, while at 72 h, both tobermorite and analcime were not observed. These results suggest that, in the CO_2-enrich environment,

Table 1
Mineralogical composition (wt%) of RE.WO_PRE, and the synthesis products of the air-based (AIR) and CO_2-based (CO_2) systems.

	RE.WO_PRE	AIR				CO_2			
	0 h	24 h	48 h	72 h	96 h	24 h	48 h	72 h	96 h
analcime	–	–	0.8 (1)	1.4 (1)	2.4 (1)	–	2.2 (1)	–	1.3 (1)
calcite	–	1.6 (1)	2.1 (1)	1.3 (1)	–	4.7 (1)	6.3 (1)	7.6 (1)	6.7 (1)
Na-P zeolite	–	–	–	–	–	2.9 (1)	5.8 (2)	6.9 (2)	5.7 (2)
Na-phillipsite	–	–	–	–	–	1.6 (1)	1.9 (1)	2.7 (2)	2.9 (2)
pyroxene	2.6 (1)	3.8 (2)	4.2 (3)	3.8 (1)	3.5 (1)	2.7 (1)	3.0 (2)	2.9 (2)	2.9 (2)
tobermorite	–	4.4 (2)	6.1 (2)	8.0 (2)	12.3 (4)	–	4.4 (1)	–	2.4 (1)
vaterite	–	4.9 (3)	5.4 (3)	5.2 (2)	–	–	–	–	–
amorphous	97.4 (1)	85.3 (2)	81.4 (2)	80.3 (2)	81.8 (1)	88.1 (1)	76.5 (2)	79.9 (1)	78.1 (1)
TZC	–	–	0.8 (1)	1.4 (1)	2.4 (1)	4.5 (1)	9.9 (1)	9.6 (1)	9.9 (1)
χ^2	0.914	1.438	1.538	1.569	1.630	1.360	1.856	1.546	1.667
R_{wp}	0.0305	0.0453	0.0466	0.0510	0.0407	0.0370	0.0435	0.0396	0.0409
R_p	0.0237	0.0352	0.0361	0.0398	0.0312	0.0286	0.0337	0.0306	0.0309

The SD (σ_Q; values in parentheses) of the weight percent of each phase (Q) was calculated from the values obtained in the output file after refinement with the GSAS software, using the formula $\sigma_{Q\ =}\ \{[\sigma_a\ a^{-1})^2 + (\sigma_b\ b^{-1})^2]^{1/2}\}$ Q where a and b are the two variables that most strongly affect Q values and refer, respectively, to the weight fraction of the phase and to the internal standard, while σ_a and σ_b are their standard deviations. "amorphous +" mainly identifies the non-crystalline phase + phases present below the detection limit. "TZC" stands for "Total Zeolitic Content". Due to structural similarities between Na-P and Na-phillipsite, their individual quantification entails a degree of uncertainty, however, the TZC remains highly reliable.

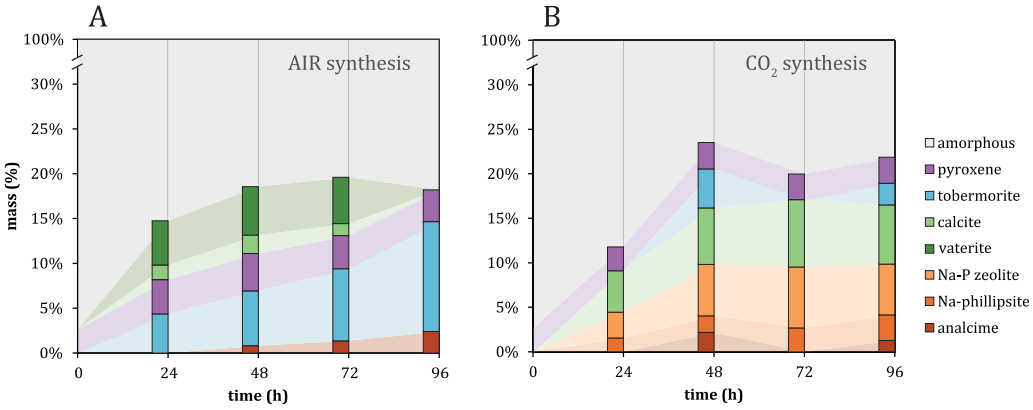

Fig. 2. Mineralogical differentiation (mass %) of the synthesis products in the AIR and CO_2 systems vs. time (h). Total bar height corresponds to product crystallinity, with segments representing distinct phase abundances. The shaded area represents a qualitative interpolation of the reaction trends; it should therefore not be interpreted as continuous data. Owing to the structural similarities of Na-P and Na-phillipsite, a certain level of uncertainty affects their individual quantification, however, their overall content is reliable.

both tobermorite and analcime were metastable intermediates subject to dissolution-reprecipitation process. Tobermorite's dissolution was plausibly due to carbonation reaction, resulting in calcite and possibly amorphous silica, as suggested by the relative increase in the amorphous matrix at 72 h, with respect to 48 h [58]. Likely, the dissolved Si and Al derived from tobermorite and analcime contributed to the synthesis of new zeolitic phases in the CO_2 system.

P-type zeolite was an important synthesis product. The zeolite P class has the general formula $M_{2/n}Al_2Si_{1.8–5.0}O_{9.6–19.0}{\cdot}5H_2O$, where M represents n-valent alkali metal cations modified from Nery et al. [59]. The framework topology corresponds to that of gismondine Framework Type Code GIS; [60], with the sodium-rich variety known as Na-P. These zeolites are often described as pseudosymmetric, as they resemble an apparent cubic structure, but possess instead lower symmetry. The maximum topological symmetry of Na-P framework corresponds to the tetragonal space group $I4_1/amd$. When crystallizing in the tetragonal system, the phase is referred to as Na-P1 [61,62]. Variants with lower symmetry crystallize in the orthorhombic (e.g., space group *Pnma*, typical of Na-P2) or in the monoclinic system; the latter is particularly observed in low-silica Na-P zeolites (e.g., space group $C2/c$ [63]). The GIS-type framework is characterized by the stacking arrangement of two-dimensional arrays of double crankshaft chains, where Na-P1 and Na-P2 isotypes differ in the relative alignment of these chains [64]. In XRPD, the most distinctive feature for their identification is the splitting of the main reflections. This characteristic was observed in the collected XRPD patterns in different samples, specifically with the appearance of a doublet at approximately 12.40 and 12.52° 2θ. However, accurately distinguishing between orthorhombic and tetragonal symmetry remains challenging due to peak broadening and pseudo-symmetry. Therefore, these phases are referred to generically as Na-P zeolites throughout the text. For the QPA, the Rietveld refinement was performed using a Na-P2 structural model [65]. The presence of Na^+ as a main exchangeable cation is consistent with the high Na content of RE.WO_PRE (approximately 6.5 wt%) and the NaOH used in the synthesis; and is confirmed by the analysis of the cations released (3.4).

In the CO_2 system, Na-P zeolite was favoured with respect to analcime, and it was recorded earlier (at 24 h), suggesting a quicker crystallization kinetic, in line with the observations of Katsuki et al. [55]. Similar observations were reported by Sathupunya et al. [66], where Na-P crystallized after 3 h while analcime appeared only after 8 h. These findings further support that the Na-P is kinetically favoured over analcime during the early stages of hydrothermal syntheses, with the latter potentially acting as a more stable, long-term phase.

It is relevant that, depending on the source material, the synthesis of GIS-type zeolites can be obtained even at lower temperatures than the 130 °C used in this work. Indeed, Srinivasan and Grutzeck [67] achieved GIS zeolites from power plant fly ash at 90 °C after 7 days of incubation, while Katz et al. [68] from nuclear waste solutions at 45–90 °C. In the

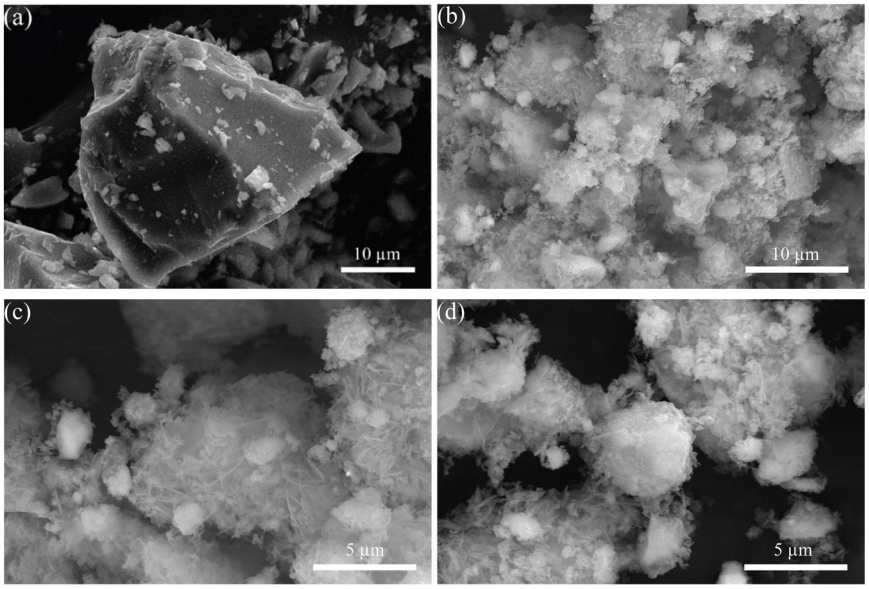

Fig. 3. SEM images of the precipitates resulted from the syntheses in air. a) RE.WO_PRE (a glass particle of approximately 40 µm is visible in the center); b) AIR_96, c) AIR_96, d) CO_2_96. The synthesis performed in air is characterized by the pervasive presence of tobermorite in the form of platy crystals, which completely coated the material.

CO_2-based synthesis, the Na-P zeolite was always associated with the synthetic analogue of phillipsite and calcite. This association is consistent with natural occurrences, where GIS-type zeolites are commonly reported in association with phillipsite and calcite [69]. From an analytical perspective, it is important to acknowledge that Na-P and phillipsite share structural similarities that can result in partially overlapping XRPD reflections. While this may introduce a degree of uncertainty in the exact quantitative partitioning between these two specific phases, the identification and quantification of the total zeolitic contents is reliable.

As already discussed, in the AIR synthesis, tobermorite was the dominant phase, arranged in layers forming a broad coating on the other mineral phases and on amorphous particles. Conversely, in the CO_2-synthesis, tobermorite was less pervasive, allowing for the morphological characterization of other amorphous (Fig. 4a) and crystalline (Fig. 4b-d) species. The largest crystals observed were analcime, reaching diameters of approximately 15–20 µm. As shown in Fig. 4b, a euhedral analcime crystal (~20 µm) rests upon a bed of elongated prismatic crystals. Point analyses and morphological characteristics suggested that this layer was constituted by phillipsite [70,71]. Moreover, the relative high Na content suggests that Na^+ was the main exchangeable cations not only for Na-P zeolite, but also phillipsite, allowing it to be referred to as Na-phillipsite.

In summary, the differences in phase composition between the AIR- and CO_2-systems are driven by the varying availability of CO_2 and its direct impact on precipitation-dissolution pathways. Since the CO_2 enrichment was conducted at ambient pressure within the limited headspace of the reaction vessels, any significant shift in the overall

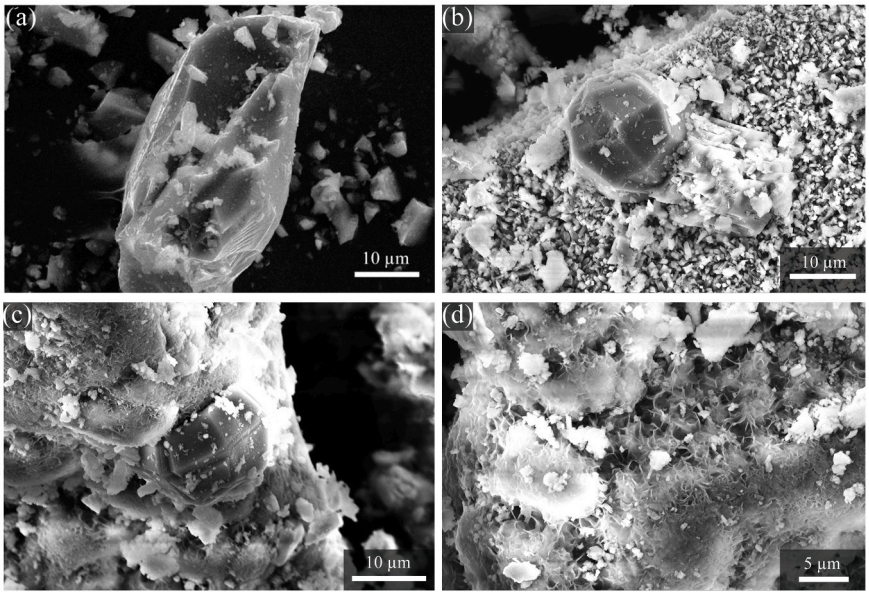

Fig. 4. SEM images of the precipitates obtained from the syntheses in the CO_2-system. a) An amorphous particle in sample RE.WO_PRE; b) CO_2_96: a fractured, euhedral analcime crystal lies beneath a bed of prismatic crystals identified as Na-phillipsite; c) CO_2_96. A twinned analcime crystal in contact with a tobermorite layer; d) CO_2_96. Detail of the tobermorite crystals with distinctive lamellar habitus and its pervasiveness on the materials surfaces.

solution pH can be reasonably ruled out. Rather, the primary mechanism relies on dissolved CO_2. In the CO_2-system, stable calcite was favoured. This precipitation acted as a calcium sink, lowering the Ca/Si ratio in the solution and thereby creating favourable conditions for the crystallization of Si-rich phases, such as zeolites.

Conversely, the lower CO_2 availability in the AIR-system led to the formation of metastable carbonates, as evidenced by the continuous fluctuation and ultimate disappearance of vaterite after 96 h. Consequently, the calcium in the system underwent continuous precipitation and redissolution, maintaining a relatively high Ca/Si ratio in the solution, ultimately shifting the thermodynamic balance in favour of tobermorite. The precipitation of zeolites was therefore limited as the formation of tobermorite consumes not only the available Ca but also Si from the solution.

3.3. Potential for CO_2 capture

Post-synthesis characterization revealed significant carbon enrichment in both the AIR and CO_2-systems, as corroborated by elemental analysis (EA). Since carbon content in RE.WO_PRE was negligible, the enrichment is attributed to the sequestration of CO_2 present inside the reaction vessels via carbonation, leading to the formation of $CaCO_3$. Notably, the highest carbon concentrations were observed in the synthesis carried out in CO_2 enriched atmosphere (Fig. 5). To investigate the potential contribution of CO_2 capture mechanisms other than mineral carbonation (the synthesis of calcite or vaterite), a mass balance was performed by comparing the carbon content measured via EA with the theoretical carbon calculated from the carbonate fraction determined by the QPA.

For AIR_24 and AIR_48, the discrepancy between measured and calculated carbon was negligible, suggesting that the captured carbon was entirely stored within crystalline carbonate phases (calcite and vaterite). In contrast, the carbon content in the samples obtained with the CO_2 synthesis consistently exceeded the stoichiometric expectations derived from QPA. This suggests that significant fraction of the carbon, ranging from 18.9 to 40.9 wt% (CO_2_24 and CO_2_96 samples, respectively), was not converted into crystalline carbonates. The most plausible mechanism to account for this discrepancy is represented by the formation of amorphous carbonates [72].

The results from the AIR-based synthesis support this hypothesis. Indeed, while mineral carbonation was identified as the dominant CO_2 capture process in AIR_24 and AIR_72, through the synthesis of calcite and vaterite, no crystalline carbonates were detected in AIR_96. Consequently, CO_2 capture in AIR_96 cannot be explained by the precipitation of crystalline phases, pointing toward fixation as amorphous fractions.

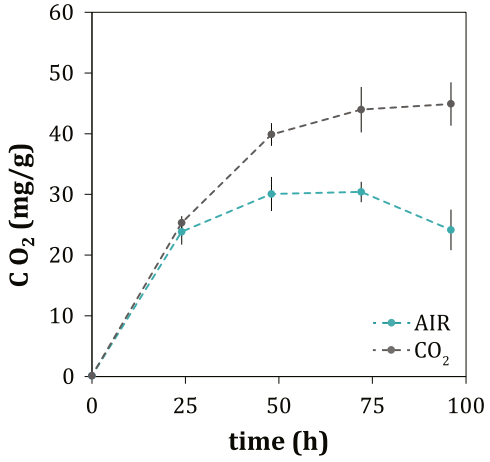

Fig. 5. Amount of CO_2 (mg/g) converted in carbonates in the synthesis products at different reaction times (h). Syntheses carried out in the CO_2-enriched atmosphere are shown in grey, while those performed in AIR are shown in light blue. Data points represent the mean of three technical replicates; SDs are represented by error bars.

In summary, concerning CO_2 capture, the hydrothermal synthesis proposed in this study, although exploratory, demonstrates significant potential for the following reasons: i) The CO_2 captured with respect to material weight reached 4.49 ± 0.36 and 2.41 ± 0.33 wt%, for the CO_2- and AIR syntheses, respectively, representing an approximately 86.0% increase in capture efficiency under the CO_2 atmosphere. ii) Samples synthesized under CO_2 exhibited superior carbon stability over time compared to those from air (Fig. 5). In fact, in AIR predominantly formed vaterite, a metastable, reactive phase of $CaCO_3$ which completely dissolved in the AIR_96 sample; in contrast, vaterite was not recorded in the CO_2 synthesis, yielding instead calcite that persisted throughout the entire synthesis duration. iii) Zeolitic yields were nearly fourfold higher in the CO_2 synthesis compared to the AIR-based system (9.85 vs 2.38 wt% TZC, respectively), highlighting the efficacy of the CO_2 atmosphere in driving framework crystallization.

3.4. Main cations released in aqueous solution and cation exchange capacity

Expected CEC values for Na-P zeolite, Na-phillipsite and analcime are approximately 460, 450, and 450 cmol(+)/kg, respectively, as estimated from the number of Al^{3+} substituting Si^{4+} in the ideal compositions of hydrated zeolites [73], normalized to the molar masses [6, 74]. Considering the amount Na-P, Na-phillipsite, and analcime recorded in AIR_96 and CO_2_96, expected CEC values were approximately 10.7 and 44.9 cmol(+)/kg, respectively. Measured CEC (based on total N contents; 2.1), well aligned with expected values (Table 2).

The CEC estimated by the main cations released in NH_4Ac were however one order magnitude higher with respect to the CEC estimated from NH_4^+-N contents, meaning that significant fractions of soluble ions were released, particularly Na^+ and Ca^{2+}. Consequently, in the proposed systems, the quantification of CEC through the measurement of Na^+, Mg^{2+}, K^+, and Ca^{2+} after their complete displacement in NH_4Ac is not reliable. In the synthesis performed in air, vaterite was likely the primary source of Ca^{2+}, followed by calcite. Both were consumed during the synthesis and completely absent in AIR_96, providing additional Ca^{2+} for the crystallization of tobermorite. Conversely, in the CO_2-system, analcime and tobermorite acted as metastable precursor phases. Their gradual dissolution-reprecipitation likely provided the Na^+ and Ca^{2+} cations necessary for the concomitant crystallization of the more stable zeolitic species. It is noteworthy that the release of Na^+ and Ca^{2+} in AIR_96 was approximately 1.5–1.6 times higher than in CO_2_96, indicating lower phase stability compared to the CO_2-system, as also suggested by XRPD data (see 3.1). CEC data further corroborate the

Table 2
Main cations released in NH_4Ac solution (cmol/kg) and CEC values (cmol(+)/kg) of the raw material used in the syntheses (RE.WO_PRE), and the two syntheses after 96 h in air (AIR_96) and CO_2 (CO_2_96). The released cations account for both exchangeable and dissolved cations (originating from mineral dissolution; e.g., vaterite). Consequently, the CEC was determined from the NH_4^+-N content of the exchanged solid samples, rather than from the dissolved cations. Values represent MEAN ± SD.

	Na^+	Mg^{2+}	K^+	Ca^{2+}	CEC
	cmol/kg				*cmol (+)/kg*
RE. WO_PRE	12.7 ± 0.3	5.10 ± 0.41	3.95 ± 0.33	40.5 ± 4.2	bdl
AIR_96	176 ± 8	5.76 ± 0.48	5.18 ± 0.61	271 ± 19	12.3 ± 0.9
CO_2_96	116 ± 7	5.00 ± 0.27	3.18 ± 0.37	166 ± 8	40.7 ± 1.6

superior performance of the CO_2 system: the higher yield of zeolitic phases in CO_2_96 with respect to in AIR_96 resulted in a CEC value approximately 3.3 times higher (40.7 ± 1.6 and 12.3 ± 0.9 cmol(+)/kg, respectively, Table 2).

3.5. Chemical characterization of the precipitates

Both AIR_96 and, particularly, CO_2_96 exhibited relatively Al enrichment compared to RE.WO_PRE precursor. Indeed, Al concentrations increased from 3.73 wt% (RE.WO_PRE) to 5.20 and 7.79 wt%, respectively (Table 3). The difference between AIR_96 and CO_2_96 was likely due to the role of CO_2 in controlling the availability of Ca^{2+} ions during the synthesis. In the CO_2 system, the dissolved Ca^{2+} was effectively removed by the crystallization of stable calcite ($CaCO_3$), which relatively suppressed the formation of tobermorite. Conversely, in the air-system, the lower concentration of CO_2 (and dissolved carbonate ions) allowed Ca^{2+} to react more effectively with silicate species to produce tobermorite. Since tobermorite consumes Si while excluding Al or incorporates only limited amount of Al^{3+} or Fe^{3+} in the so-called Al-substituted tobermorite [75], its precipitation effectively competed with zeolite crystallization [50]. This competitive consumption likely resulted in a product by a higher residual Si/Al ratio and a concomitant lower zeolite content. The Si/Al ratio indeed decreased from 5.98 (RE.WO_PRE) to 4.48 (AIR_96) and 2.84 (CO_2_96), respectively. Physicochemical conditions are recognized as key factors in determining the shifts of the Si/Al ratio during zeolites synthesis [76]. In this work, the only variability was due to different CO_2 contents and partial pressures between the AIR and CO_2 systems.

Comparison with prior analyses of RE.WO batches reveal measurable compositional variability. RE.WO_PRE showed higher Na (6.49 vs. 2.63 wt%), lower Mg (4.05 vs. 6.15 wt%) and higher Ca (16.6 vs. 11.5 wt%) relative to Arletti et al. [3]. This variability is intrinsic to *End-of-Waste* derived products due to feedstock heterogeneity and processing differences; while it should be acknowledged, it is consistent with expected batch-to-batch variation and is not expected to compromise the general validity of the findings. Replicate batch analyses would further quantify this variability.

Concerning other elements, sulfur exhibited a marked depletion in both AIR_96 and CO_2_96 compared to RE.WO_PRE, suggesting that sulfur species were subject to strong dissolution. Conversely, AIR_96 showed a relative enrichment in several elements of environmental concern, specifically Cd, Pb, and Sb. However, noteworthy such enrichment was not observed in the CO_2 synthesis, highlighting a further advantage of the CO_2 system.

4. Conclusions

This study investigated the potential for simultaneous zeolite synthesis and CO_2 capture through a preliminary laboratory-scale process using inert waste glass derived from rock wool under low-temperature conditions. The CO_2-based synthesis proved superior to the air-based system across all evaluated parameters, driven by the following key factors: i) The yield of zeolitic phases was significantly higher, accompanied by a superior cation exchange capacity; ii) The process effectively demonstrated CO_2 sequestration potential in the form of stable carbonates; conversely, in the air-based synthesis, carbonates were either fully dissolved or amorphized after 96 h. Moreover, the zeolites formed in the CO_2 system offer an additional pathway for CO_2 sequestration via physisorption mechanisms; iii) From an environmental perspective, the chemical composition of the CO_2-synthesis products revealed no significant deviations from the starting material, whereas the air-based synthesis suggested a relative enrichment in potential contaminants. Although the recovered zeolite content in the best-case scenarios remained relatively low (around 10%), and the CO_2 fixation capacity was relatively low compared to other carbonation systems, this study demonstrates that processes coupling simultaneous zeolite synthesis and CO2 fixation at low temperatures are potentially feasible and efficient.

The CO_2 dissolved in the crystallization medium may control the crystallization products obtained. By driving the carbonation reactions between stable and metastable carbonates (e.g., calcite and vaterite) CO_2 plausibly controlled the evolution of the available Ca/Si ratio, directly determining whether the system favoured the crystallization of tobermorite or zeolites.

the concurrent production of zeolites and CO_2 sequestration is a promising approach. Further research could elevate the proposed process to competitive Technology Readiness Levels. Future studies should focus on testing the system under significantly higher CO_2 pressures, higher temperatures (evaluating the use of recycled heat from the production plant of RE.WO) as well as evaluating the effects of specific reagents and catalysts. In summary, this approach demonstrated the potential to valorise an *End-of-Waste* product, transforming it into high-valuable resources in full alignment with circular economy principles.

CRediT authorship contribution statement

Malferrari Daniele: Writing – review & editing, Methodology, Investigation, Funding acquisition, Conceptualization. **Gualtieri Alessandro Francesco:** Writing – review & editing, Supervision, Resources, Funding acquisition, Conceptualization. **GALAMINI Giulio:** Writing – original draft, Methodology, Investigation, Formal analysis, Data curation.

Table 3
Chemical composition of RE.WO Elements listed in the left part are reported as a mass percentage (%), while those in the right are in mg/kg. Elements marked with "*" were measured by WDXRF (one replicate). Values are expressed as MEAN ± SD of three replicates.

Element *(%)*	RE.WO_PRE	AIR_96	CO_2_96	Element *(mg/kg)*	RE.WO_PRE	AIR_96	CO_2_96
Na	6.49 ± 0.33	6.61 ± 0.48	6.51 ± 0.29	**S***	1075	202	230
Mg	4.05 ± 0.26	3.89 ± 0.38	4.49 ± 0.33	**Cl***	192	306	305
Al*	3.73	5.20	7.79	**V**	130 ± 4	130 ± 15	81.9 ± 2.5
Si*	22.3	23.3	22.1	**Cr**	421 ± 19	576 ± 69	424 ± 12
K	0.938 ± 0.057	0.930 ± 0.090	0.817 ± 0.037	**Co**	25.8 ± 0.4	33.9 ± 3.9)	26.2 ± 1.3
Ca	16.6 ± 1.0	16.4 ± 1.6	18.1 ± 0.9	**Ni**	223 ± 33	273 ± 42	219 ± 16
B	0.351 ± 0.019	0.344 ± 0.008	0.340 ± 0.003	**Cu**	240 ± 13	308 ± 32	243 ± 11
P	0.114 ± 0.015	0.122 ± 0.011	0.123 ± 0.009	**As**	2.53 ± 1.05	2.29 ± 0.25	2.12 ± 0.35
Mn	0.317 ± 0.022	0.350 ± 0.012	0.442 ± 0.016	**Sr***	515	135	271
Fe	8.48 ± 0.47	8.39 ± 0.87	10.2 ± 0.3	**Mo**	25.5 ± 2.0	29.7 ± 4.4	17.6 ± 3.0
Ti	0.641 ± 0.024	0.785 ± 0.067	0.752 ± 0.166	**Cd**	0.736 ± 0.010	1.06 ± 0.10	0.750 ± 0.019
Zn	0.104 ± 0.006	0.118 ± 0.003 (44)	0.102 ± 0.005	**Sb**	11.5 ± 1.6	19.7 ± 3.3	11.7 ± 1.1
Zr*	0.132	0.178	0.118	**Pb**	29.5 ± 1.9	41.5 ± 6.4	29.5 ± 0.8
				Ce*	108	187	163

Funding

This work was funded under i) the PNRR-M4C2INV1.5, NextGenerationEU-Avviso 3277/2021-ECS_00000033-ECOSISTER-spk1; ii) Project 101113855 LIFE22-ENV-IT-LIFE: RE.WO, REcycling mineral WOol waste into high-value products.

Declaration of Competing Interest

The authors declare that they have no known competing financial interests or personal relationships that could have appeared to influence the work reported in this paper.

Acknowledgements

We gratefully thanks Zanotti s.r.l. for the samples of RE.WO used in the paper.

Data availability

Data will be made available on request.

References

[1] World Health Organization (WHO), Determination of airborne fibre number concentrations: A recommended method, by phase-contrast optical microscopy (Membrane Filter Method), World Health Organization, Geneva, 1997. ISBN 9241544961.
[2] European Commission, Communication from the Commission to the European Parliament, the European Council, the Council, the European Economic and Social Committee and the Committee of the Regions: The European Green Deal, COM (2019) 640 final, Brussels (2019).
[3] R. Arletti, S. Conte, C. Zanelli, M. Iuliis, D. Giuseppe, V. Scognamiglio, D. Malferrari, M. Dondi, A. Gualtieri, Recycling the product of thermal inertization of man-made vitreous fibres for the manufacture of stoneware tiles, Waste Biomass. Valoriz. 14 (2022) 1–16, https://doi.org/10.1007/s12649-022-01959-8.
[4] I. Zannatto, A. Gualtieri, Apparato per il trattamento di rifiuti contenenti lana minerale, 102021000002246 (2021).
[5] M. Sisti, D. Guidetti, F. Altimari, F. Andreola, L. Barbieri, I. Lancellotti, L. Casini, F. Colombo, R. Arletti, R. Fantini, A.F. Gualtieri, Sustainable glazes for ceramic tiles: exploiting inertized man-made vitreous fibres waste as a resource, Ceram. Int. 51 (2025) 4195–4205, https://doi.org/10.1016/j.ceramint.2024.11.396.
[6] G. Gottardi, E. Galli, Natural Zeolites, Minerals and Rocks 18 (1985), https://doi.org/10.1007/978-3-642-46518-5.
[7] R.T. Pabalan, F.P. Bertetti, Cation-exchange properties of natural zeolites, Rev. Mineral. Geochem. 45 (2001) 453–518, https://doi.org/10.2138/rmg.2001.45.14.
[8] S. Eren, F.N. Türk, H. Arslanoğlu, Synthesis of zeolite from industrial wastes: a review on characterization and heavy metal and dye removal, Environ. Sci. Pollut. Res. 31 (2024) 41791–41823, https://doi.org/10.1007/s11356-024-33863-0.
[9] S. Buzukashvili, R. Sommerville, W. Hu, O. Brooks, O. Kökkılıç, P. Ouzilleau, N. A. Rowson, K.E. Waters, Zeolite synthesis from coal fly ash and its application to heavy metals remediation from water contaminated with Pb, Cu, Zn and Ni ions, Miner. Eng. 209 (2024) 108619, https://doi.org/10.1016/j.mineng.2024.108619.
[10] B. Makgabutlane, L.N. Nthunya, E.N. Nxumalo, N.M. Musyoka, S.D. Mhlanga, Microwave irradiation-assisted synthesis of zeolites from coal fly ash: an optimization study for a sustainable and efficient production process, ACS Omega 5 (2020) 25000–25008, https://doi.org/10.1021/acsomega.0c00931.
[11] W. Ma, Y. Yi, M. Fang, C. Li, J. Li, W. Liu, Study on the synthesis mechanism of sodalite, gismondine, and zeolite-P1 zeolite materials from ladle furnace slag and fly ash, Sci. Rep. 13 (2023) 3232, https://doi.org/10.1038/s41598-023-30282-y.
[12] N.S. Samanta, M.K. Purkait, Preparation of zeolite by green synthesis from steel industry by-product LD-slag and its application for photodegradation, Mater. Res. Bull. 190 (2025) 113492, https://doi.org/10.1016/j.materresbull.2025.113492.
[13] D. Kubatova, M.K. Kotlanova, I. Khongova, A. Zezulova, M. Bohac, Use the waste glass for the synthesis of geopolymer-zeolite composites, J. Phys. Conf. Ser. 2341 (2022) 012012, https://doi.org/10.1088/1742-6596/2341/1/012012.
[14] M. Sayehi, G. Delahay, H. Tounsi, Synthesis and characterization of ecofriendly materials zeolite from waste glass and aluminum scraps using the hydrothermal technique, J. Environ. Chem. Eng. 10 (2022) 108561, https://doi.org/10.1016/j.jece.2022.108561.
[15] W.M. Xie, F.P. Zhou, X.L. Bi, D.D. Chen, J. Li, S.Y. Sun, J.Y. Liu, X.Q. Chen, Accelerated crystallization of magnetic 4A-zeolite synthesized from red mud for application in removal of mixed heavy metal ions, J. Hazard. Mater. 358 (2018) 441–449, https://doi.org/10.1016/j.jhazmat.2018.07.007.
[16] G. Ke, H. Shen, P. Yang, Synthesis of X-Zeolite from waste basalt powder and its influencing factors and synthesis mechanism, Materials 12 (2019) 3895, https://doi.org/10.3390/ma12233895.
[17] Y.L. Zhu, Z.H. Chang, J. Pang, C.J. Xiong, Synthesis of zeolite 4A from kaolin and bauxite by alkaline fusion at low temperature, Mater. Sci. Forum 685 (2011) 298–306, https://doi.org/10.4028/www.scientific.net/MSF.685.298.
[18] M.A. Klunk, S.B. Schröpfer, S. Dasgupta, M. Das, N.R. Caetano, A.N. Impiombato, P.R. Wander, C.A.M. Moraes, Synthesis and characterization of mordenite zeolite from metakaolin and rice husk ash as a source of aluminium and silicon, Chem. Pap. 74 (2020) 2481–2489, https://doi.org/10.1007/s11696-020-01095-4.
[19] Q. Zhou, X. Jiang, Q. Qiu, Y. Zhao, L. Long, Synthesis of high-quality NaP1 zeolite from municipal solid waste incineration fly ash by microwave-assisted hydrothermal method and its adsorption capacity, Sci. Total Environ. 855 (2023) 158741, https://doi.org/10.1016/j.scitotenv.2022.158741.
[20] Z. Chen, G. Song, C. Li, W. Chen, Z. Li, S. Kawi, Coal fly ash to Y zeolite of great purity and crystallinity: a new and green activation method of combined in situ microwave and ultrasound, Solid State Sci. 136 (2023) 107102, https://doi.org/10.1016/j.solidstatesciences.2022.107102.
[21] L. Velarde, M.S. Nabavi, E. Escalera, M.-L. Antti, F. Akhtar, Adsorption of heavy metals on natural zeolites: a review, Chemosphere 328 (2023) 138508, https://doi.org/10.1016/j.chemosphere.2023.138508.
[22] M. Alberghini, G. Ferretti, G. Galamini, C. Botezatu, B. Faccini, Selective ammonium recovery from livestock and organic solid waste digestates using zeolite tuff: efficiency and farm-scale prospects, Recycling 10 (2025) 137, https://doi.org/10.3390/recycling10040137.
[23] V. Gadore, S.R. Mishra, N. Yadav, G. Yadav, Md Ahmaruzzaman, Advances in zeolite-based materials for dye removal: current trends and future prospects, Inorg. Chem. Commun. 166 (2024) 112606, https://doi.org/10.1016/j.inoche.2024.112606.
[24] N. Jiang, R. Shang, S.G.J. Heijman, L.C. Rietveld, High-silica zeolites for adsorption of organic micro-pollutants in water treatment: a review, Water Res. 144 (2018) 145–161, https://doi.org/10.1016/j.watres.2018.07.017.
[25] W. Lu, C. Zhang, P. Su, X. Wang, W. Shen, B. Quan, Z. Shen, L. Song, Research progress of modified natural zeolites for removal of typical anions in water, Environ. Sci. Water Res. Technol. 8 (2022) 2170–2189, https://doi.org/10.1039/D2EW00478J.
[26] L. Kustov, S. Dunaev, A. Kustov, Nitrous oxide adsorption and decomposition on zeolites and zeolite-like materials, Molecules 27 (2022) 398, https://doi.org/10.3390/molecules27020398.
[27] J. Lee, J. Kim, K.Y. Park, J.B. Joo, S. Bae, Enhanced and prolonged adsorption of ammonia gas by zeolites derived from coal fly ash, Chemosphere 368 (2024) 143799, https://doi.org/10.1016/j.chemosphere.2024.143799.
[28] N. Li, W. Liu, L. Liu, P. Gao, Q. Wu, X. Ma, G.K. Li, Evaluation of gas adsorption and separation performance of binder-free Y zeolite particles prepared by the rotary pelletization method, Sep. Purif. Technol. 361 (2025) 131520, https://doi.org/10.1016/j.seppur.2025.131520.
[29] Z. Tahir, A. Ilyas, X. Li, M. Bilad, I. Vankelecom, A. Khan, Tuning the gas separation performance of fluorinated and sulfonated PEEK membranes by incorporation of zeolite 4A, J. Appl. Polym. Sci. 135 (2017), https://doi.org/10.1002/app.45952.
[30] L. Morrone, L. Neri, O. Facini, G. Galamini, G. Ferretti, A. Rotondi, Influence of chabazite zeolite foliar applications used for olive fruit fly control on volatile organic compound emission, photosynthesis, and quality of extra virgin olive oil, Plants 13 (2024) 698, https://doi.org/10.3390/plants13050698.
[31] G. Ferretti, M. Alberghini, G. Galamini, V. Medoro, B. Faccini, S. Balzan, M. Coltorti, Exploring the combined effects of different nitrogen sources and chabazite zeolite-tuff on nitrogen dynamics in an acidic sandy-loam soil, Soil Syst. 8 (2024) 16, https://doi.org/10.3390/soilsystems8010016.
[32] G. Galamini, D. Malferrari, F. Altimari, S. Orlandi, L. Barbieri, From quarry by-products to a zeolites-based Zn fertilizer with increased resistance to rain leaching, Microporous Mesoporous Mater. 379 (2024) 113290, https://doi.org/10.1016/j.micromeso.2024.113290.
[33] M. Napolitano, G. Malavasi, D. Malferrari, G. Galamini, M. Catauro, V. Viola, F. Marani, L. Barbieri, A new high-efficiency fertilization system from waste materials for soil protection: material engineering, chemical-physical characterization, antibacterial and agronomic performances, Materials 18 (2025) 3492, https://doi.org/10.3390/ma18153492.
[34] A.I. Hadi, A. Yan, Y. Hu, B. Lin, T. Zhou, D. Ouyang, J. Tang, A comprehensive review of carbon capture: from conventional to emerging electrochemical technologies, Energy 9 (2025) 100415, https://doi.org/10.1016/j.nxener.2025.100415.
[35] United Nations Framework Convention on Climate Change (UNFCCC), The Paris Agreement (2016).
[36] Intergovernmental Panel on Climate Change (IPCC), Climate Change 2023: Synthesis Report, Intergovernmental Panel on Climate Change (IPCC) (2023), https://doi.org/10.59327/IPCC/AR6-9789291691647.
[37] International Energy Agency (IEA), World Energy Outlook (2025).
[38] X. Lin, X. Li, H. Liu, G. Boczkaj, Y. Cao, C. Wang, A review on carbon storage via mineral carbonation: bibliometric analysis, research advances, challenges, and perspectives, Sep. Purif. Technol. 338 (2024) 126558, https://doi.org/10.1016/j.seppur.2024.126558.
[39] R. Baciocchi, G. Costa, M. Di Gianfilippo, A. Polettini, R. Pomi, A. Stramazzo, Thin-film versus slurry-phase carbonation of steel slag: CO2 uptake and effects on mineralogy, J. Hazard. Mater. 283 (2015) 302–313, https://doi.org/10.1016/j.jhazmat.2014.09.016.
[40] Z. Tong, G. Ma, D. Zhou, G. Yang, C. Peng, The indirect mineral carbonation of electric arc furnace slag under microwave irradiation, Sci. Rep. 9 (2019) 7676, https://doi.org/10.1038/s41598-019-44162-x.
[41] S. Tian, J. Jiang, X. Chen, F. Yan, K. Li, Direct gas–solid carbonation kinetics of steel slag and the contribution to in situ sequestration of flue gas CO2 in steel-

making plants, ChemSusChem 6 (2012) 2348–2355, https://doi.org/10.1002/cssc.201300436.
[42] G. Hu, S. Rohani, X. Jiang, J. Li, Q. Liu, W. Liu, CO2 mineral sequestration and faujasite zeolite synthesis by using blast furnace slag: process optimization and CO2 net-emission reduction evaluation, ACS Sustain. Chem. Eng. 9 (2021), https://doi.org/10.1021/acssuschemeng.1c05576.
[43] S. Shin, M.-J. Kim, Hydrothermal synthesis of zeolites from residual waste generated via indirect carbonation of coal fly ash, Sustain. Environ. Res. 34 (2024), https://doi.org/10.1186/s42834-023-00206-6.
[44] ISO, ISO 13320:2020. Particle size analysis — Laser diffraction methods, International Organization for Standardization, Geneva, Switzerland (2020).
[45] A.C. Larson, R.B. Von Dreele, B. Toby, General structure analysis system - GSAS/EXPGUI, Los Alamos National Laboratory, Rep. LAUR 86 (1994) 748.
[46] B. Toby, A graphical user interface for GSAS, J. Appl. Crystallogr. 34 (2001) 210–213, https://doi.org/10.1107/S0021889801002242.
[47] A.F. Gualtieri, G.D. Gatta, R. Arletti, G. Artioli, P. Ballirano, G. Cruciani, A. Guagliardi, D. Malferrari, N. Masciocchi, P. Scardi, Quantitative phase analysis using the Rietveld method: towards a procedure for checking the reliability and quality of the results, Period. di Mineral. 88 (2019), https://doi.org/10.2451/2019PM870.
[48] W.H. Hendershot, M. Duquette, A simple barium chloride method for determining cation exchange capacity and exchangeable cations, Soil Sci. Soc. Am. J. 50 (1986) 605–608, https://doi.org/10.2136/sssaj1986.03615995005000030013x.
[49] C. Biagioni, S. Merlino, E. Bonaccorsi, The tobermorite supergroup: a new nomenclature, Mineral. Mag. 79 (2015) 485–495, https://doi.org/10.1180/minmag.2015.079.2.22.
[50] D. Malferrari, G. Galamini, M. Bernini, R. Fantini, G. Malvolti, A.F. Gualtieri, Kinetic investigation of tobermorite synthesis for the recovery of carcinogenic respirable crystalline silica (RCS), ACS Omega (2025), https://doi.org/10.1021/acsomega.5c06547.
[51] D. Malferrari, F. Bernini, D. Di Giuseppe, V. Scognamiglio, A.F. Gualtieri, Al-substituted tobermorites: an effective cation exchanger synthesized from “End-of-Waste” materials, ACS Omega 7 (2022) 1694–1702, https://doi.org/10.1021/acsomega.1c04193.
[52] I. Jiménez, G. Pérez, A. Guerrero, B. Ruiz, Mineral phases synthesized by hydrothermal treatment from biomass ashes, Int. J. Miner. Process. 158 (2017) 8–12, https://doi.org/10.1016/j.minpro.2016.11.002.
[53] Y. Guo, X. Pan, Q. Liu, H. Yu, Hydrothermal synthesis and formation mechanism of lightweight tobermorite from industrial lime and water glass, J. Sustain. Met. 11 (2025) 3105–3116, https://doi.org/10.1007/s40831-025-01188-y.
[54] B. Lothenbach, D. Jansen, Y. Yan, J. Schreiner, Solubility and characterization of synthesized 11 Å Al-tobermorite, Cem. Concr. Res. 159 (2022) 106871, https://doi.org/10.1016/j.cemconres.2022.106871.
[55] K. Katsuki, H. Suzuki, M. Hasegawa, M. Heike, N. Hosomachi, Y. Yamashita, Y. Nakamura, Effect of reaction temperature on Fe–Al analcime formation, J. Porous Mater. 14 (2007) 443–448, https://doi.org/10.1007/s10934-006-9038-6.
[56] J. Kawano, N. Shimobayashi, M. Kitamura, K. Shinoda, N. Aikawa, Formation process of calcium carbonate from highly supersaturated solution, J. Cryst. Growth 237–239 (2002) 419–423, https://doi.org/10.1016/S0022-0248(01)01866-8.
[57] S.Y.M.H. Seepma, S.E. Ruiz-Hernandez, G. Nehrke, K. Soetaert, A.P. Philipse, B.W. M. Kuipers, M. Wolthers, Controlling CaCO3 Particle Size with {Ca2+}:{CO32–} Ratios in Aqueous Environments, Cryst. Growth Des. 21 (2021) 1576–1590, https://doi.org/10.1021/acs.cgd.0c01403.
[58] M. Izadifar, C. Natzeck, K. Emmerich, P.G. Weidler, S. Gohery, C. Burvill, P. Thissen, Unexpected chemical activity of a mineral surface: the role of crystal water in tobermorite, J. Phys. Chem. C. 126 (2022) 12405–12412, https://doi.org/10.1021/acs.jpcc.1c10151.
[59] J.G. Nery, Y.P. Mascarenhas, A.K. Cheetham, A study of the highly crystalline, low-silica, fully hydrated zeolite P ion exchanged with (Mn2+, Cd2+, Pb2+, Sr2+, Ba2+) cations, Microporous Mesoporous Mater. 57 (2003) 229–248, https://doi.org/10.1016/S1387-1811(02)00594-2.
[60] S. Hansen, U. Håkansson, L. Fälth, Structure of synthetic zeolite Na-P2, Acta Crystallogr. Sect. C. 46 (1990) 1361–1362, https://doi.org/10.1107/S010827018901262X.
[61] Ch Baerlocher, W.M. Meier, The crystal structure of synthetic zeolite Na-P 1, an isotype of gismondine, Z. F. üR. Krist. - Cryst. Mater. 135 (1972) 339–354, https://doi.org/10.1524/zkri.1972.135.16.339.
[62] S. Hansen, U. Håkansson, A.R. Landa-Canovas, L. Falth, On the crystal chemistry of NaP zeolites, Zeolites 13 (1993) 276–280, https://doi.org/10.1016/0144-2449(93)90006-O.
[63] B.R. Albert, A.K. Cheetham, J.A. Stuart, C.J. Adams, Investigations on P zeolites: synthesis, characterisation, and structure of highly crystalline low-silica NaP, Microporous Mesoporous Mater. 21 (1998) 133–142, https://doi.org/10.1016/S1387-1811(97)00059-0.
[64] J. Al Atrach, A. Aitblal, A. Amedlous, Y. Xiong, M. Desmurs, V. Ruaux, R. Guillet-Nicolas, V. Valtchev, Nanosized zeolite P for enhanced CO2 adsorption kinetics, ACS Appl. Mater. Interfaces 16 (2024) 38006–38016, https://doi.org/10.1021/acsami.4c05988.
[65] L.B. McCusker, C. Baerlocher, R. Nawaz, Rietveld refinement of the crystal structure of the new zeolite mineral gobbinsite, Z. F. üR. Krist. Cryst. Mater. 171 (1985) 281–290, https://doi.org/10.1524/zkri.1985.171.14.281.
[66] M. Sathupunya, E. Gulari, S. Wongkasemjit, ANA and GIS zeolite synthesis directly from alumatrane and silatrane by sol-gel process and microwave technique, J. Eur. Ceram. Soc. 22 (2002) 2305–2314, https://doi.org/10.1016/S0955-2219(02)00042-0.
[67] A. Srinivasan, M.W. Grutzeck, The adsorption of SO2 by zeolites synthesized from fly ash, Environ. Sci. Technol. 33 (1999) 1464–1469, https://doi.org/10.1021/es9802091.
[68] A. Katz, A.R. Brough, R.J. Kirkpatrick, L.J. Struble, J.F. Young, Effect of solution concentration on the properties of a cementitious grout wasteform for low-level nuclear, Waste 129 (2000) 236–245.
[69] G. Gottardi, E. Galli, Natural Zeolites, Geological Magazine, Minerals and Rocks Series 18 (2009) 718, https://doi.org/10.1017/S0016756800024456.
[70] M. Hussein, K. Ibrahim, S. Musleh, Characterization of raw zeolite and surfactant-modified zeolite and their use in removal of selected organic pollutants from water, Int. J. Chem. Sci. 12 (2014) 815–844.
[71] D. Novembre, D. Gimeno, M. Calista, V. Mancinelli, E. Miccadei, On the suitability of phillipsite-chabazite zeolitite rock for ammonia uptake in water: a case study from the Pescara River (Italy), Sci. Rep. 12 (2022) 9284, https://doi.org/10.1038/s41598-022-13367-y.
[72] J.D. Rodriguez-Blanco, S. Shaw, L.G. Benning, The kinetics and mechanisms of amorphous calcium carbonate (ACC) crystallization to calcite, viavaterite, Nanoscale 3 (2011) 265–271, https://doi.org/10.1039/C0NR00589D.
[73] International Zeolite Association (IZA), Index of Natural Zeolites Datasheets, http://www.iza-online.org/natural/ (accessed 11.12.25).
[74] V.J. Inglezakis, The concept of “capacity” in zeolite ion-exchange systems, J. Colloid Interface Sci. 281 (2005) 68–79, https://doi.org/10.1016/j.jcis.2004.08.082.
[75] S. Diamond, J.L. White, W.L. Dolch, Effects of isomorphous substitution in hydrothermally-synthesized tobermorite, Am. Mineral. 51 (1966) 388–401.
[76] J. Li, M. Gao, W. Yan, J. Yu, Regulation of the Si/Al ratios and Al distributions of zeolites and their impact on properties, Chem. Sci. 14 (2023) 1935–1959, https://doi.org/10.1039/D2SC06010H.